New Journal of Physics
The open access journal at the forefront of physics

Deutsche Physikalische Gesellschaft DPG IOP Institute of Physics

The cosmic ray energy spectrum as measured using the Pierre Auger Observatory

To cite this article: Giorgio Matthiae 2010 *New J. Phys.* **12** 075009

New Journal of Physics
The open-access journal for physics

The cosmic ray energy spectrum as measured using the Pierre Auger Observatory

Giorgio Matthiae
University of Roma 'Tor Vergata' and Sezione INFN, Roma, Italy
E-mail: matthiae@roma2.infn.it

New Journal of Physics **12** (2010) 075009 (24pp)
Received 15 October 2009
Published 9 July 2010
Online at http://www.njp.org/
doi:10.1088/1367-2630/12/7/075009

Abstract. The Auger Observatory was designed to study high-energy cosmic rays by measuring the properties of the showers produced in the atmosphere. The instrument has taken data since January 2004 and was completed in 2008. First results on the energy spectrum of the primary cosmic rays for energies above 10^{18} eV with statistics larger than collected in previous works are presented and discussed.

Contents

1. Introduction

The flux of primary cosmic rays, as it was known in the year 2000, is shown in figure 1 as a function of energy. It follows approximately a power law $E^{-\gamma}$ with spectral index γ roughly equal to 3.

In the region above 10^{19} eV, which is being explored in detail by the Auger collaboration, the flux of the primaries is extremely low, of the order of only one particle per km^2 per century near 10^{20} eV. Therefore the study of cosmic rays in this very-high-energy region requires detectors with very large acceptance.

The recent compilation of figure 2 clearly demonstrates the remarkable improvement that has been achieved in the last decade when relatively large amounts of data have been collected. The spectrum exhibits interesting features, usually called the 'knee' and the 'ankle'. At the energy of the 'knee' ($\sim 3 \times 10^{15}$ eV), the spectral index changes approximately from 2.7 to 3.1. The word 'ankle' refers to another change of the slope around a few 10^{18} eV. It has been actively studied together with the suppression that is evident at the far end of the spectrum. These features will be discussed in section 5, where the new data from the Auger collaboration will be presented.

It should be noted that presenting the data as flux multiplied by a power of the energy ($E^{2.5}$ in figure 2) is quite usual because the features that are not very evident in a normal plot of the flux versus energy become more visible. However, it has the disadvantage of coupling the horizontal and vertical axes, thus enhancing the differences in the energy calibration of the different experiments.

In figures 1 and 2, the equivalent centre-of-mass (c.m.) system energy for proton–proton collisions at high-energy accelerating machines is also indicated.

2. Historical background

It was earlier realized [3] that protons with energy above a few 10^{19} eV have to come from extragalactic sources because their gyration radius in the galactic magnetic field is of the same order as the size of our galaxy, and therefore containment is not possible and no acceleration mechanism could be effective. In fact the gyration radius of a particle with charge Z can be written as

$$R_{\mathrm{g}} = 100\,\mathrm{kpc} \times (E/10^{20}\,\mathrm{eV}) \times (1\,\mu G/B)/Z,$$

where E is the particle energy and B the intensity of the regular magnetic field, which in our galaxy is of the order of 1 μG. This remark was put in a quantitative way in [4], where the acceleration potentialities of various astrophysical systems are discussed on the basis of the two relevant parameters, the size and magnetic field of the accelerating region. Obviously, for given values of these two parameters, the acceleration of nuclei with higher Z is in principle easier.

Classical acceleration models are generally derived from the original Fermi's ideas of acceleration by moving clouds of magnetized plasma and shock waves from a supernova explosion. These models quite naturally predict a power-law spectrum for the production at the source. However, the actual mechanism of particle acceleration above a few 10^{19} eV still remains mysterious.

A crucial step forward in gaining further knowledge of the far end of the energy spectrum was made by the observation in 1962 of an event with energy in excess of 10^{20} eV at the Volcano Ranch surface array [5]. Afterwards, several other collaborations claimed to have recorded

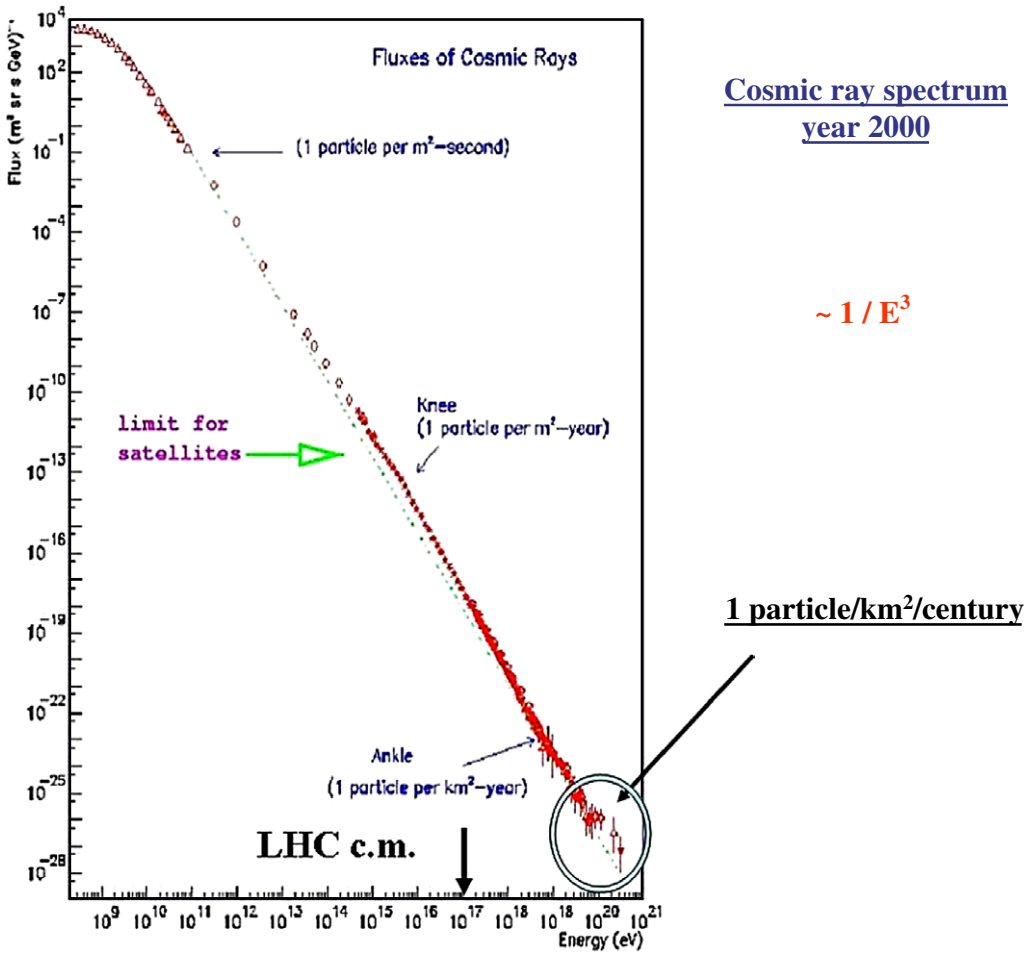

Figure 1. Early compilation of the flux of primary cosmic rays as a function of energy [1].

events with energy close to or above 10^{20} eV, as discussed in great detail in the comprehensive review [6], which describes the state-of-the-art on the study of high-energy cosmic rays during the year 2000.

An important feature of the spectrum in the energy region above 10^{19} eV is a mechanism suggested by Greisen and by Zatsepin and Kuz'min [7] that is known as GZK suppression. This is due to the interactions of the cosmic rays with the low-energy photons of the cosmic microwave background (CMB) and was suggested soon after the discovery of the CMB. Protons with energy above the effective threshold for photoproduction of pions ($\sim 4 \times 10^{19}$ eV) will lose energy as they travel in space, as shown in figure 3.

Another way of representing the effect of interaction of protons with the CMB is shown in figure 4.

It is quite clear that the actual energy spectrum as measured at the Earth's surface will generally be quite different from the original production spectrum and will depend on the actual distance of the source.

These considerations lead to the notion of GZK horizon. Protons emitted with very high energy could be observed at the Earth's surface only if the source is not too distant. As the

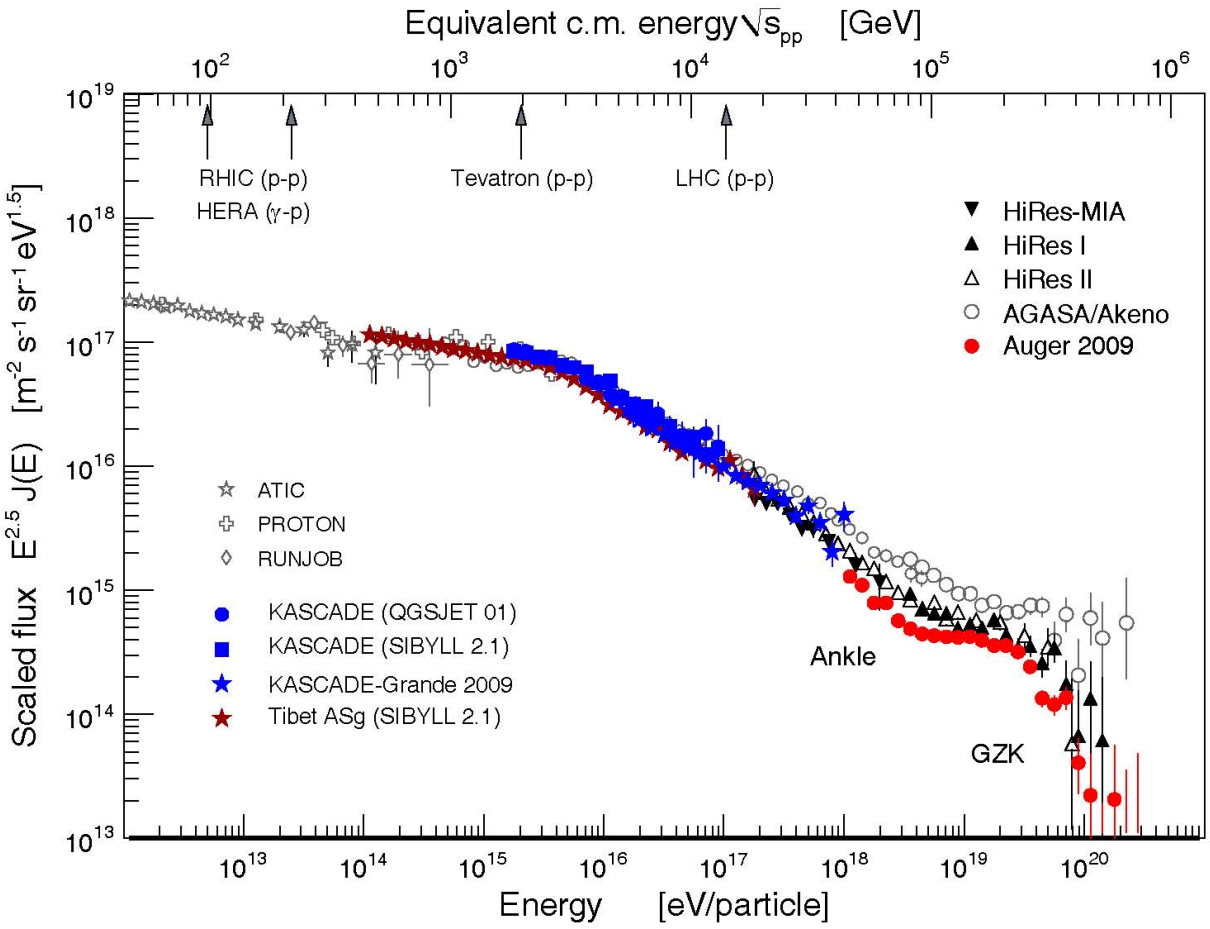

Figure 2. Recent compilation of the cosmic ray energy spectrum [2]. The flux is multiplied by the power law $E^{2.5}$.

observed energy increases, the radius of the GZK 'sphere' shrinks. With 90% probability, protons with energy above 5×10^{19} eV must have come from a distance shorter than 250 Mpc, while the corresponding figure for protons with energy above 10^{20} eV is about 75 Mpc.

The effect of the interaction of protons with the CMB has been studied in detail. The interaction length (mean free path for interaction) and the attenuation length, defined as the distance corresponding to attenuation of the proton energy by a factor e on average, are shown in figure 5.

As shown in figure 5, the interaction length for pion production is of the order of 10 Mpc above 10^{20} eV and the energy loss per interaction is about 15–20%.

A relevant quantity is the value of the energy $E_{1/2}$, where the integral spectrum of protons would be reduced to one half as a consequence of the interaction with the CMB. Numerically, $E_{1/2}$ was predicted [9] to be $10^{19.76}$ eV (corresponding to about 5.5×10^{19} eV), almost independent of the power-law spectrum at the production. It is therefore a signature of the GZK cutoff.

Production of electron–positron pairs is also present, but it is much less effective than pion production in terms of reduction of the proton energy (see figure 5). However, if the spectrum is totally dominated by protons, this process is predicted ([10] and references therein) to be

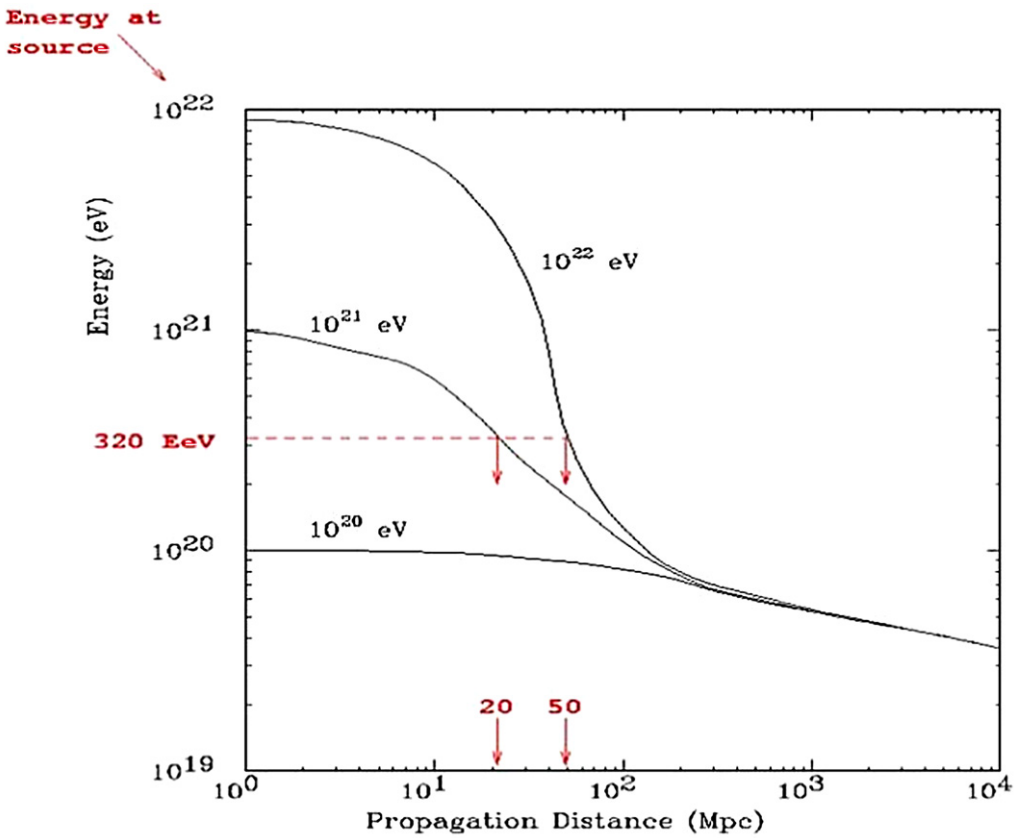

Figure 3. The energy of protons as a function of the propagation distance [8]. As a consequence of the GZK effect, protons coming from a distance greater than ∼100 Mpc have lost memory of their initial energy.

responsible for the feature related to the ankle, i.e. the shallow minimum (or 'dip'), in the plot of the flux times E^3, which is centered at energies of a few 10^{18} eV.

The spectrum of the CMB, the cross sections of pion photoproduction and the Bethe–Heitler cross section of electron–positron production by photons on protons are well known. As a consequence, calculations of the propagation of protons in space are quite reliable ([11] and references therein). The use of Monte Carlo simulation techniques also enables the fluctuations in the final energy (assuming, for example, a mono-energetic production spectrum) to be evaluated. The energy loss being a stochastic process, large fluctuations are expected for not too distant sources when the number of independent interaction events is small.

A convenient way of illustrating the effect of the GZK mechanism is provided by the modification factor, which is the energy-dependent function that is multiplied to an assumed shape of the production spectrum in order to obtain the predicted spectrum at the Earth's surface. An example taken from [10] is shown in figure 6, where the effects of the production of electron–positron pairs and of pions are shown separately. According to this calculation, pion photoproduction causes the expected GZK suppression, while electron–positron production is responsible for the shape of the ankle. The results are almost independent of the spectral index γ_g of the spectrum at the source.

Traditionally, the GZK mechanism is meant to refer to the proton interaction with the CMB. However, a similar mechanism exists also when the primaries are nuclei. Apparently, the most

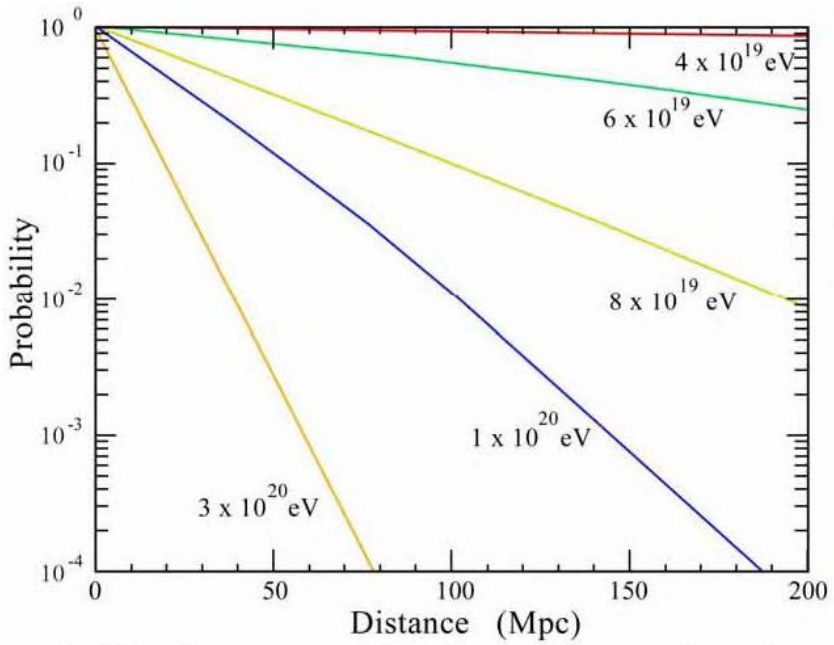

Figure 4. The survival probability of protons of a given energy at the source as a function of the distance traveled.

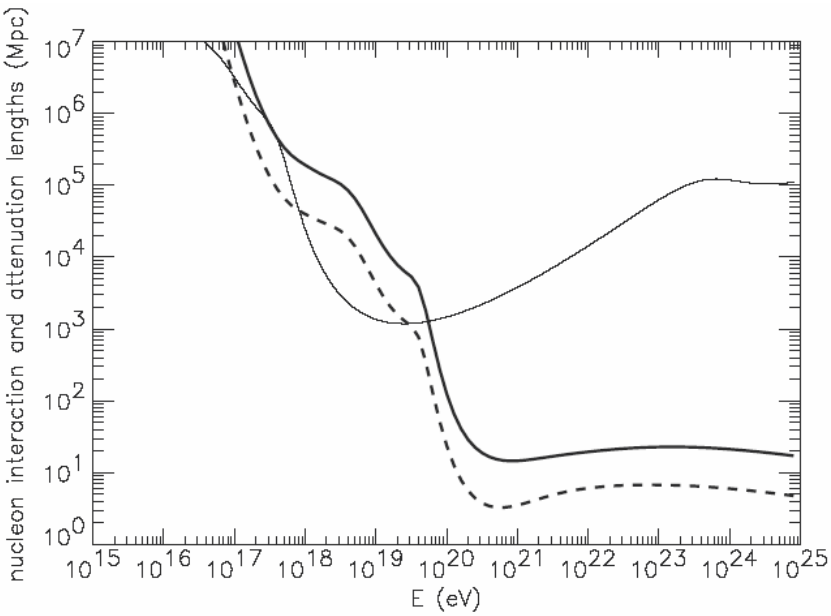

Figure 5. The interaction length (dashed line) and the attenuation length (thick solid line) for photoproduction of pions by high-energy protons interacting with the photons of the CMB are shown as a function of the proton energy. The interaction length for production of electron–positron pairs (thin solid line) is also shown.

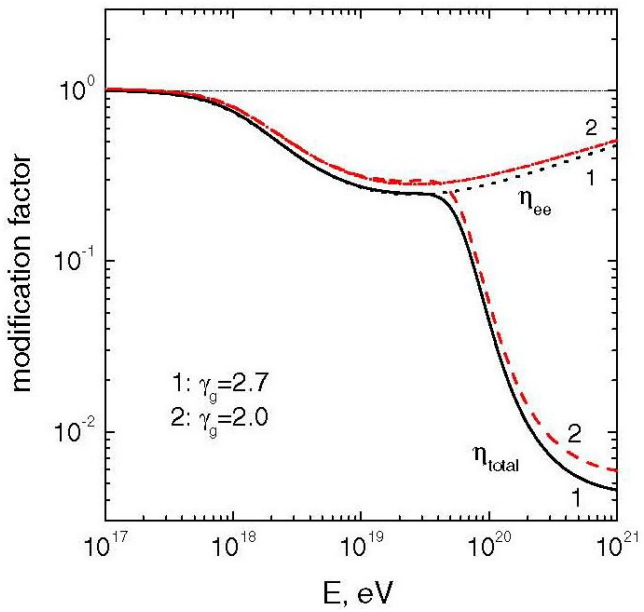

Figure 6. Modification factor due to e^+e^- production and to pion photoproduction for the energy spectrum of protons with two different values of the assumed spectral index γ_g at the accelerating sources. 1. $\gamma_g = 2.7$. Dotted line: e^+e^- production. Black solid line: all energy losses, including pion photoproduction. 2. $\gamma_g = 2.0$. Red solid line: e^+e^- production. Dashed line: all energy losses, including pion photoproduction. Above $\sim 5 \times 10^{19}$ eV, the energy losses are dominated by pion photoproduction.

important effect is due to the interaction with the background photons in the infrared, visible and ultraviolet parts of the spectrum. Most relevant is the energy region of the giant dipole resonance (GDR), where the cross section is large when the photon energy (for the nuclei relevant in the present discussion) is around 20–25 MeV in the nucleus rest frame. The most important reactions are (γ, n) and (γ, p), while ejection of more than one nucleon is less probable.

It is clear that the GZK mechanism for nuclei is much more complex than that for protons. Primary nuclei will not only suffer energy degradation but also undergo a kind of 'stripping', with reduction of the mass number, as they propagate in space. This effect appears to be quite important for nuclei lighter than iron. In addition, realistic calculations must also take into account the β decay of the nuclear fragments. As a consequence of this complex chain of events, the mass composition as observed at the Earth's surface might be quite different from the mass spectrum at the production source. The problem has been discussed by various authors (see, for example, [12, 13] and reference therein), but it is likely to require more detailed investigations.

At present, a large amount of nuclear physics data on the GDR are available. Presumably, thorough use of these data in astrophysical calculations would be of great help in order to clarify this issue.

The modification factors for primaries of pure mass composition, He and Fe nuclei, as calculated in [10], are shown in figure 7. While for He the GZK effect is at an energy one order of magnitude below that for protons, for iron nuclei the GZK suppression appears accidentally at about the same energy as for protons. The picture for CNO nuclei is similar to that for He.

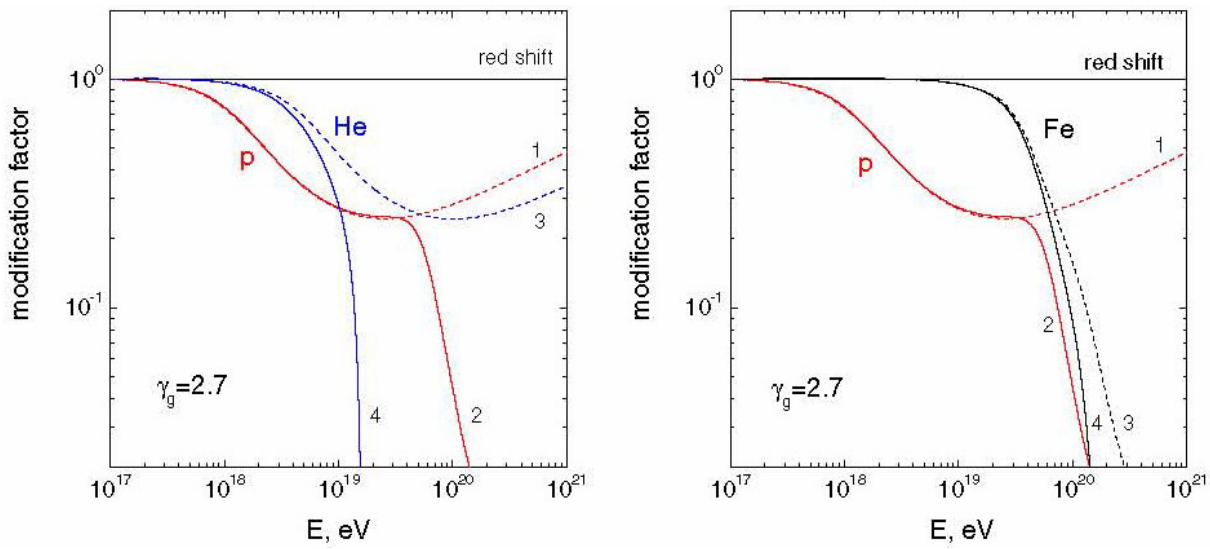

Figure 7. Modification factor due to e^+e^- production (dotted line) and to pion production (solid line) for the energy spectrum of He (left panel) and Fe nuclei (right panel) for an assumed power index $\gamma_g = 2.7$ at the acceleration sources. The results for a pure proton composition (already shown in figure 6) are also reported here for comparison.

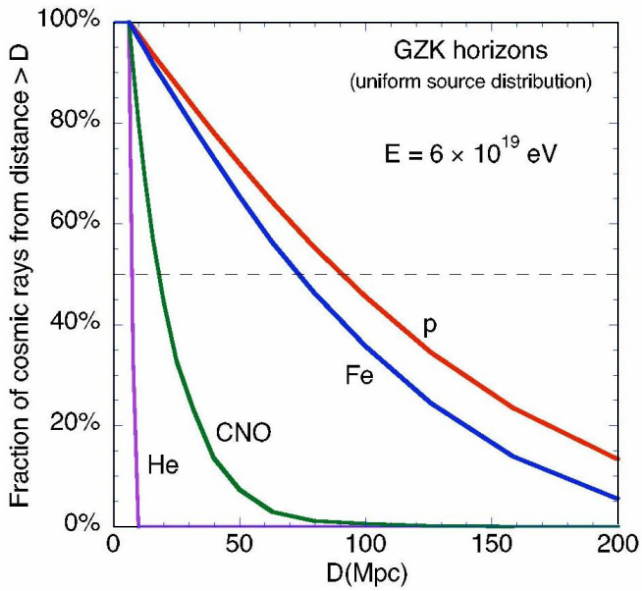

Figure 8. The survival fraction of primary cosmic rays of different mass and the energy 6×10^{19} eV as a function of the distance of the source from the Earth [14].

Results of the calculations reported in [14] and shown in figure 8 seem to indicate that only protons and iron nuclei have the probability of surviving after traveling from 'distant' sources, while light nuclei, such as He, C, N and O, are easily destroyed.

In the past, there was a controversy about the actual presence of the suppression predicted by the GZK mechanism. The AGASA [15] data did not show a suppression, contrary to the

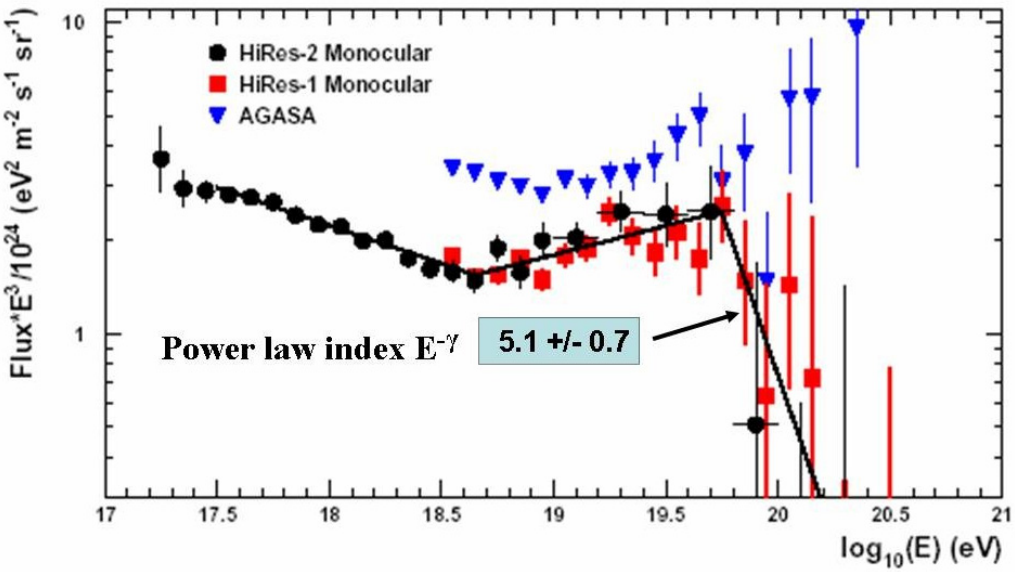

Figure 9. The final HiRes results on the energy spectrum are presented as Flux $\times E^3$ and compared with the earlier AGASA data. The steepening due to the GZK cutoff is clearly seen. In addition, the ankle, which in this plot appears as a shallow minimum centered on $10^{18.6}$ eV, is also evident.

preliminary data of HiRes. The experimental situation is now clarified by the final data of HiRes [16], shown in figure 9, and by the data of Auger (figure 2 and section 5). The HiRes data clearly show a suppression of the spectrum above $10^{19.6}$ eV with a fitted value of the spectral index $\gamma = 5.1 \pm 0.7$. The energy at which the steepening is observed agrees with the expectations from the GZK cutoff.

The difference between the AGASA and HiRes data can hardly be attributed to the limited statistics. While AGASA is a surface array and the energy calibration is based on theoretical models and simulations, HiRes and Auger measure the energy of the showers directly with a calorimetric method based on the fluorescence technique, and therefore the disagreement is most likely due to a systematic difference in the energy assignment.

There seems to be general consensus that, in the region between the knee and ankle, there is a transition between galactic and extragalactic origin of the primary cosmic rays. The events at the far end of the spectrum are believed to be of extragalactic origin. However, the actual description of the transition is model dependent [17], as shown in figure 10 taken from (see [18] and references therein). Model uncertainty could be reduced by gaining a knowledge of the mass composition.

From the brief historical review of this section, one may draw the following conclusions:

- There must be a transition from galactic to extragalactic origin in the region between the knee and ankle. The events at the end of the spectrum are of extragalactic origin.
- A limitation on the maximum acceleration energy can be foreseen for any galactic and extragalactic system assumed to be a source of very-high-energy cosmic rays.
- The GZK suppression for protons is well understood theoretically, while the suppression for nuclei is a much more complex mechanism not yet fully understood.

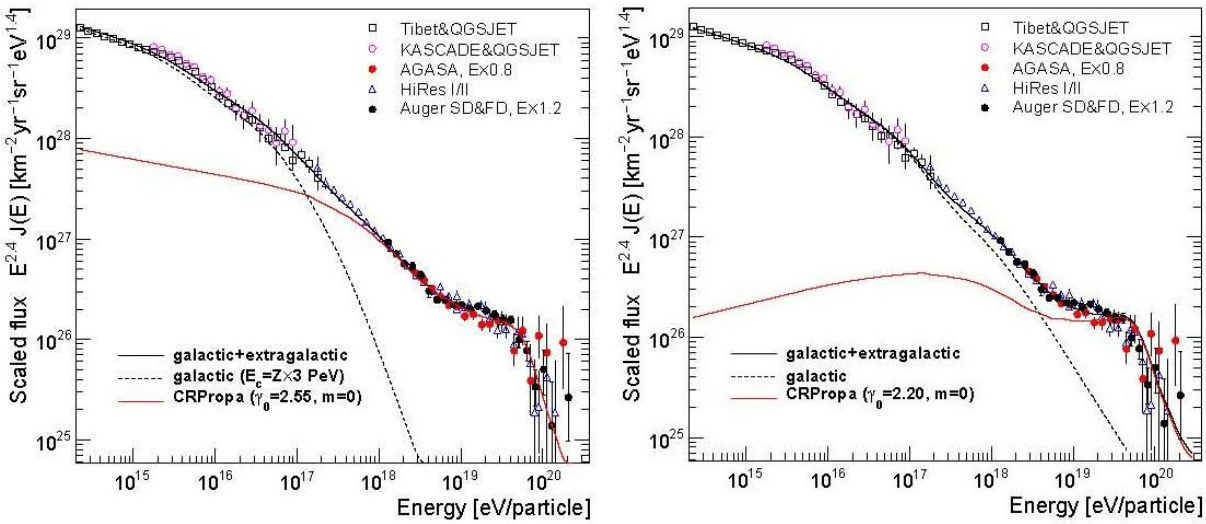

Figure 10. Examples of two different (and extreme) models of the galactic (dotted line) and extragalactic (red line) contributions. In the left panel, the transition occurs around 10^{17} eV, whereas in the right panel the transition is at the ankle, i.e. at an energy more than one order of magnitude higher. The quantity γ_g is the spectral index at the source and $m = 0$ indicates that the sources are assumed to be uniformly distributed in space.

- The HiRes data and the first data from Auger show a suppression at the energy where the GZK effect is predicted.
- The suppression at the end of the spectrum could reveal a limitation on the acceleration power of the sources, but the GZK effect has to be there anyway for 'distant' sources if most particles are accelerated to energies of the order of and above 10^{20} eV.
- The shape of the energy spectrum and the mass composition as measured at the Earth's surface are the result of a complex combination of the production mechanism and propagation effects.

Much better insight into the process of production and propagation of the primary cosmic rays should be provided by the data that the Auger Observatory has already started to collect and will continue to accumulate in the next decade.

3. The Auger Observatory

The setting up of two observatories, one in the Northern hemisphere and another in the Southern hemisphere, is foreseen in the Auger project, so to achieve a full exploration of the sky. The proposed Northern Observatory [19] will be built in Colorado (USA). The Southern Auger Observatory [20], completed in 2008, is located near the small town of Malargüe in the province of Mendoza (Argentina) at a latitude of about 35 °S and an altitude of 1400 m above sea level. The region, called 'Pampa amarilla', is flat with a very low population density and favorable atmospheric conditions. The observatory is a hybrid system: a combination of a large surface array and a fluorescence detector (see figure 11).

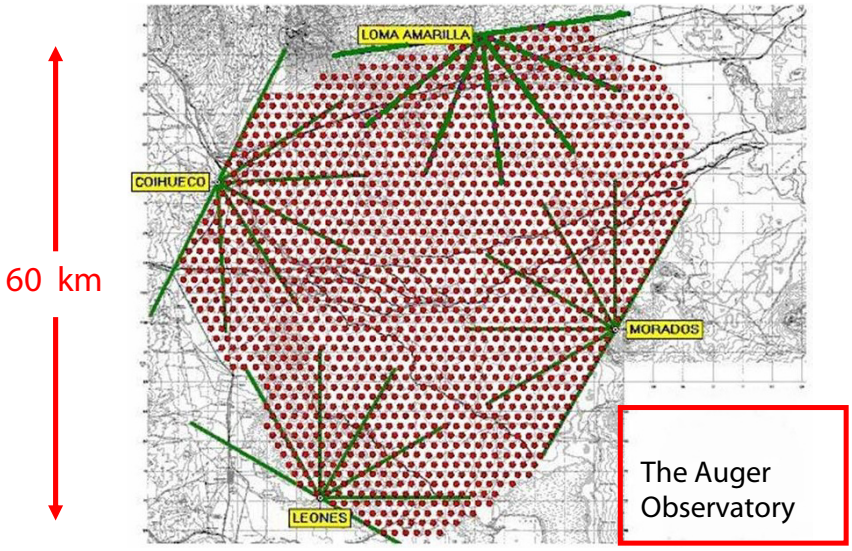

Figure 11. Sketch of the site of the Auger Observatory. Each red dot represents a water Cherenkov detector. The four fluorescence sites on the perimeter of the surface array are also indicated, together with their horizontal field of view.

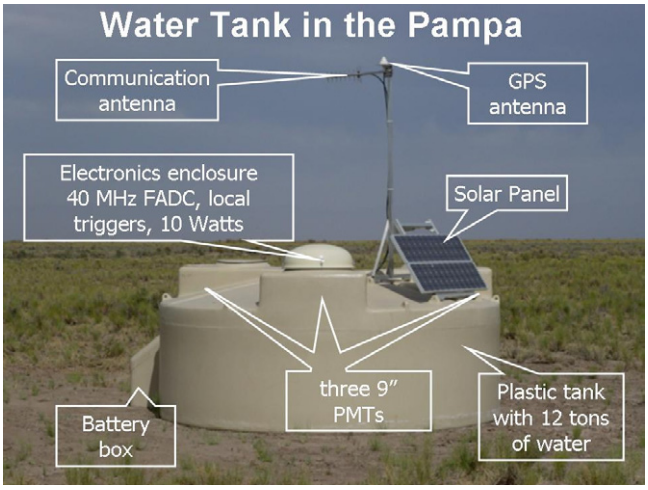

Figure 12. Picture of a water tank of the SD of the Auger Observatory. The insets give explanations of the various components of the system, which is autonomous with a battery and a solar panel. Signal digitization is carried out locally and the result is transmitted via radio. Synchronization is achieved by the GPS system.

3.1. The surface detector (SD)

The SD is a large array of more than 1600 water Cherenkov detectors spaced at a distance of 1.5 km and covering a total area of 3000 km^2. Each detector is a plastic tank of cylindrical shape with size 10 m^2 $\times$ 1.2 m filled with purified water [21]. Technical details of a tank are given in figure 12. The SD measures the front of the shower as it reaches the ground. The tanks activated by a cosmic ray shower record the particle density and the time of arrival.

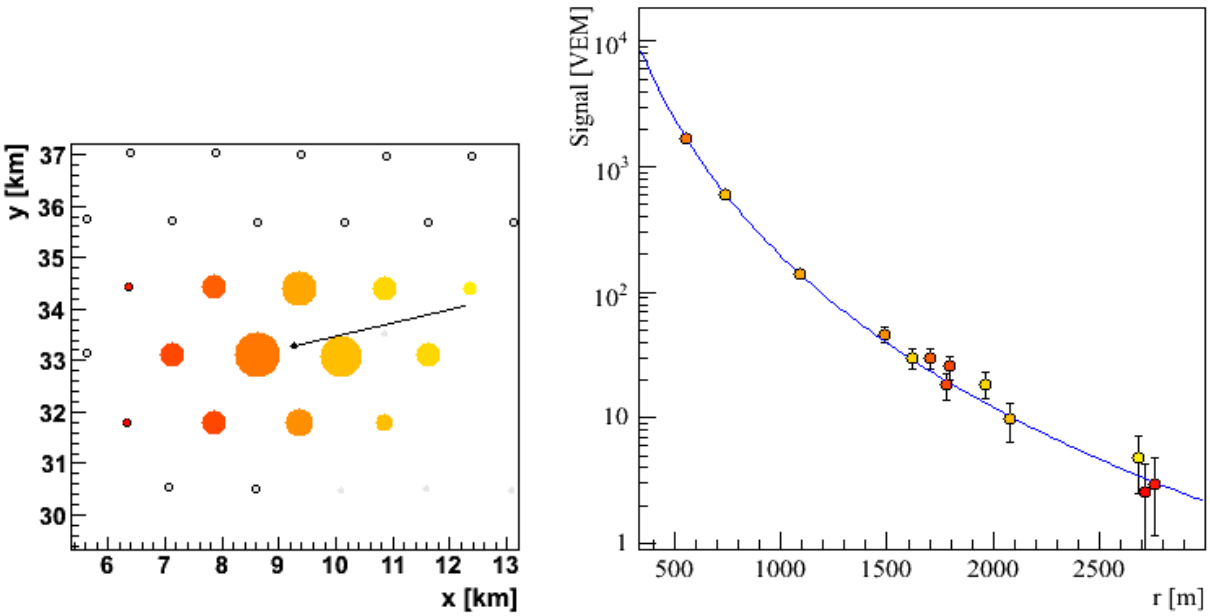

Figure 13. Example of an event of high energy as observed by the SD. As shown in the left panel, the shower has activated 13 water Cherenkov detectors distributed over an area of about 20 km^2. The activated tanks are indicated by colored circles. Following the usual conventions, the radius of the circles is proportional to the logarithm of the observed signals, which are plotted in the right panel as a function of the distance r from the reconstructed shower axis. The signals expressed in units of VEM are shown together with the results of the LDF fit.

An example of a high-energy event, as observed by the SD, is shown in figure 13. The signal of each water Cherenkov detector is expressed in units of vertical equivalent muons (VEM), which represents the signal produced by a muon traversing the tank vertically.

The flux of cosmic ray muons provides continuous monitoring of the SD. From the magnitude and the timing of the signals of the tanks, one derives the direction of the axis of the shower and the point of impact on the ground.

The right panel of figure 13 shows the signal S, expressed in units of VEM as a function of the distance r from the shower axis. The dependence of S on the distance r is described with a simple analytical expression known as the lateral distribution function (LDF), which is fitted to the data. The following empirical form of the type originally proposed by Nishimura, Kamata and Greisen (the NKG formula) [22] has been used:

$$S = A[r/r_s(1 + r/r_s)]^{-\beta},$$

where $r_s = 700$ m. The parameters A and β are determined from the fit. Numerically, β is in the range 2–2.5 at energies greater than $\sim 10^{19}$ eV.

The fit provides a value of the signal that would be observed at a distance of 1000 m from the shower axis. This interpolated quantity, $S(1000)$, is a good energy estimator in the sense that it is well correlated with the energy of the primary [23]. The choice of 1000 m is not critical and is related to the spatial separation between the individual detectors of the surface array. Other

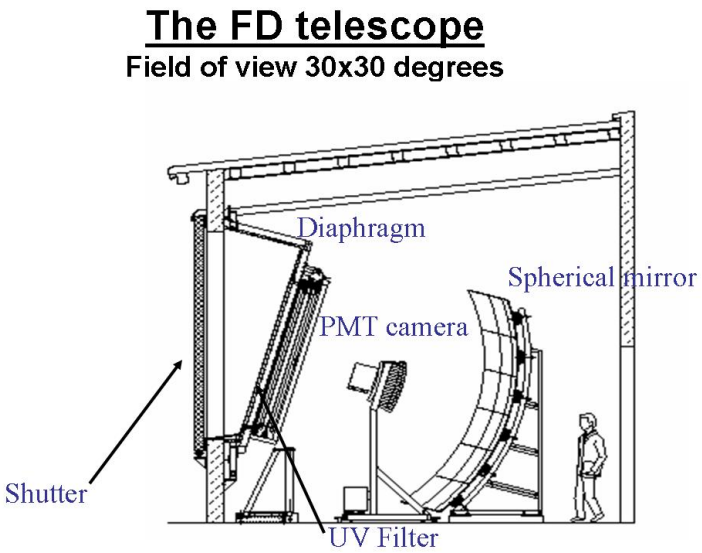

Figure 14. Sketch of a fluorescence telescope. The main components are indicated.

instruments, such as AGASA or Haverah Park, with smaller separation between the detectors have used $S(600)$ as the energy estimator [6].

3.2. The fluorescence detector (FD)

The FD of the Auger Observatory (described in detail in [24]) consists of 24 telescopes located in four stations, which are built on small elevations on the perimeter of the site. The telescopes measure the longitudinal development of the showers by observing the fluorescence light produced by the interaction of the charged particles of the showers with the nitrogen molecules of the atmosphere.

Each telescope has a 12 m^2 spherical mirror with a curvature radius of 3.4 m and a camera with 440 photomultipliers. The field of view of each telescope is $30^\circ \times 30^\circ$. UV filters placed on the diaphragm reject light outside the 300–400 nm emission spectrum of the fluorescence. The FD may operate only in clear moonless nights and therefore with an uptime of about 13%. A sketch of a telescope is shown in figure 14.

The fluorescence technique was successfully pioneered by the Fly's Eye group of the University of Utah [25]. The method relies on a knowledge of the fluorescence yield and its dependence on pressure and temperature.

Details of the properties of emission of fluorescence light by nitrogen molecules of the atmosphere are given in [26], where the final results of different experiments are converted to a suitable unit, Y_{337}, defined as the number of fluorescence photons produced at the main emission band of 337 nm per unit energy deposited in the air by the shower particles at a pressure of 1013 hPa and a temperature of 293 K.

The Auger collaboration has used the absolute fluorescence yield reported in [27], $Y_{337} = 5.0$ photons MeV^{-1}. This value is close to the average of different experiments, which differ by about $\pm 10\%$. A Monte Carlo simulation ([26] and reference therein) suggests a correction to the result of Nagano *et al* [27], leading to the value $Y_{337} = 5.5$ photons MeV^{-1}.

The absolute calibration [24, 28] of the FD telescopes is done using accurately calibrated light sources and a cylindrical diffuser that illuminate the camera uniformly. It is an end-to-end procedure that takes into account the transmission of the filter, the reflectivity of the mirror and the response of the camera photomultipliers.

Some rather complex and sophisticated equipment for monitoring the atmosphere has been installed on the site of the Auger Observatory. This system, based on the LIDAR technique and on steerable laser beams, provides continuous information about the attenuation of the fluorescence light due to Rayleigh and aerosol scattering along the path from the shower to the telescopes [24, 29].

The measurement of the longitudinal profile of the showers is based on the empirical formula of Gaisser and Hillas, which gives the number of particles $N(x)$ as a function of the atmospheric depth x in the following form with four independent parameters:

$$N(x) = N_{\max}\left(\frac{x - x_0}{x_{\max} - x_0}\right)^{(x_{\max} - x_0/\Lambda)} \exp\left(\frac{x_{\max} - x}{\Lambda}\right).$$

The quantity x_0 is related to the depth of the first interaction in the atmosphere, $x_{\max}$ is the depth where the shower reaches the maximum, $N(x_{\max}) = N_{\max}$, and the parameter Λ controls the development of the shower.

The energy deposited by the shower particles as a function of the depth is obtained from the observed light profile by solving a set of equations describing contributions of both fluorescence and Cherenkov light.

The fluorescence technique is based on the use of the atmosphere on the observatory site as a kind of gigantic calorimeter, where the emitted fluorescence light is proportional to the energy deposited in the air by the charged particles of the showers. The Gaisser–Hillas fit provides a measurement of the total track length.

Examples of reconstructed longitudinal profiles of showers are shown in figure 15.

The calorimetric measurement of the energy provided by the fluorescence technique has to be corrected for the missing energy essentially due to muons and neutrinos, which are not contributing to the observed energy. The correction, evaluated with simulation programs, is small and rather well known, as shown in figure 16, where the ratio of the primary cosmic ray energy to the visible energy is plotted as a function of energy for two different types of primaries (protons and Fe nuclei) and for different simulation programs.

At 10^{19} eV the correction is about 8 and 12% for protons and Fe nuclei, respectively. At present, the average of protons and Fe nuclei has been used. The corresponding uncertainty is not the main source of error in the actual measurement of the energy. However, eventually, for improved precision, a knowledge of the mass composition will be relevant.

4. The energy calibration

The assignment of the energy to the showers observed with a surface array has been a long-standing problem in cosmic ray physics. It requires realistic simulation of the basic parameters of hadronic interactions in energy regions that are well above those explored with accelerating machines.

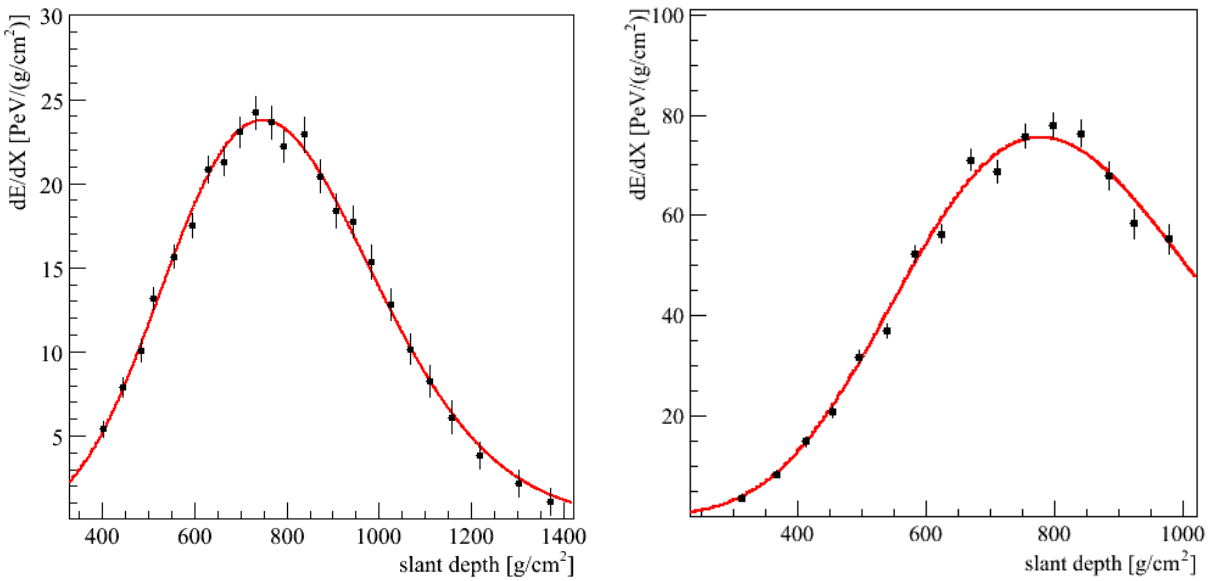

Figure 15. Examples of longitudinal profiles of high-energy showers as measured by the FD. The energy deposited by the particles of the shower is plotted as a function of the atmospheric slant depth. The quoted angles refer to the observed shower axis as obtained from the reconstruction program. Left panel: energy $\approx 1.5 \times 10^{19}$ eV, zenith angle $\approx 55°$. Right panel: energy $\approx 4.5 \times 10^{19}$ eV, zenith angle $\approx 36°$.

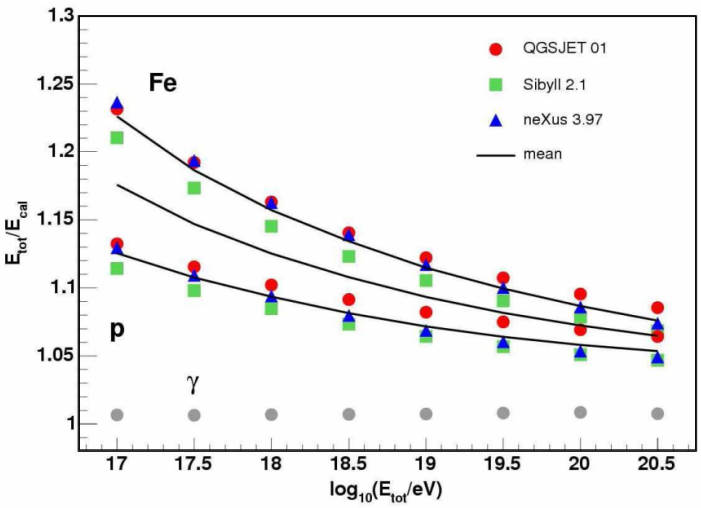

Figure 16. Ratio of the primary energy to the observed calorimetric energy for different primary species, Fe nuclei, protons and photons, according to different simulation programs. The two solid lines represent mean values for Fe nuclei and protons.

Relying on simulations may introduce large systematic uncertainty, which is also hard to estimate.

In addition, the conversion from the measured value of $S(1000)$ to the primary energy would depend on the choice of the simulation program.

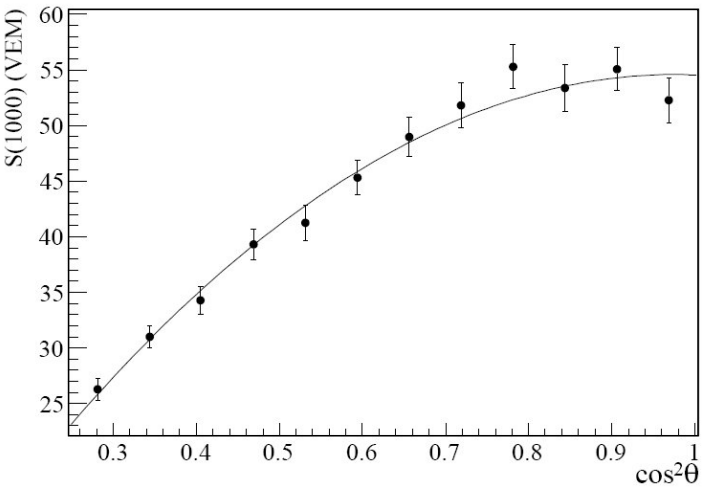

Figure 17. Example of the dependence of $S(1000)$ on the zenith angle. The line is the result of a fit with a quadratic function of $\cos^2\theta$. The data refer to $S_{38} =$ 47 VEM, which corresponds to an energy of about 10^{19} eV.

For these reasons, the Auger collaboration decided to assign the shower energy in an almost model-independent way, exploiting the hybrid nature of the observatory using the data itself rather than simulations [30].

While the main data used for the energy spectrum are provided by the surface detector, which has an uptime close to 100%, the energy calibration is based on the calorimetric measurement obtained from the fluorescence telescopes, which operate with uptime of only about 13%.

For each event, the energy estimator $S(1000)$ is obtained as discussed in section 3.1. The energy estimator $S(1000)$ depends on the zenith angle because the effective atmosphere thickness seen by showers before reaching the ground changes with the zenith angle. The value of $S(1000)$ corresponding to the median zenith angle of 38° is used as a reference and the zenith angle dependence of the energy estimator is determined, assuming that the arrival directions are distributed isotropically. This procedure is traditionally called 'Constant Intensity Cut' [31].

The zenith angle dependence of $S(1000)$ is shown in figure 17.

The absolute calibration of $S(1000)$ is obtained from the hybrid events using the calorimetric energy measured by the FD, which is then corrected for the missing energy (neutrinos and muons) using the mean value between proton and iron (see figure 16).

A sample of 795 hybrid events of good quality was selected to establish the correlation between the FD energy E_{FD} and the energy estimator S_{38}. This correlation is shown in figure 18.

In the energy region where the surface array is fully efficient, $E > 3 \times 10^{18}$ eV, the correlation between S_{38} and E_{FD} is well described by the power law [30]:

$$E_{\mathrm{FD}} = a[S_{38}]^b.$$

The numerical values of the parameters a and b obtained by fitting this expression to the data are

$$a = \{1.51 \pm 0.06\ (\mathrm{stat}) \pm 0.12\ (\mathrm{syst})\} \times 10^{17}\ \mathrm{eV},$$

$$b = 1.07 \pm 0.01\ (\mathrm{stat}) \pm 0.04\ (\mathrm{syst}).$$

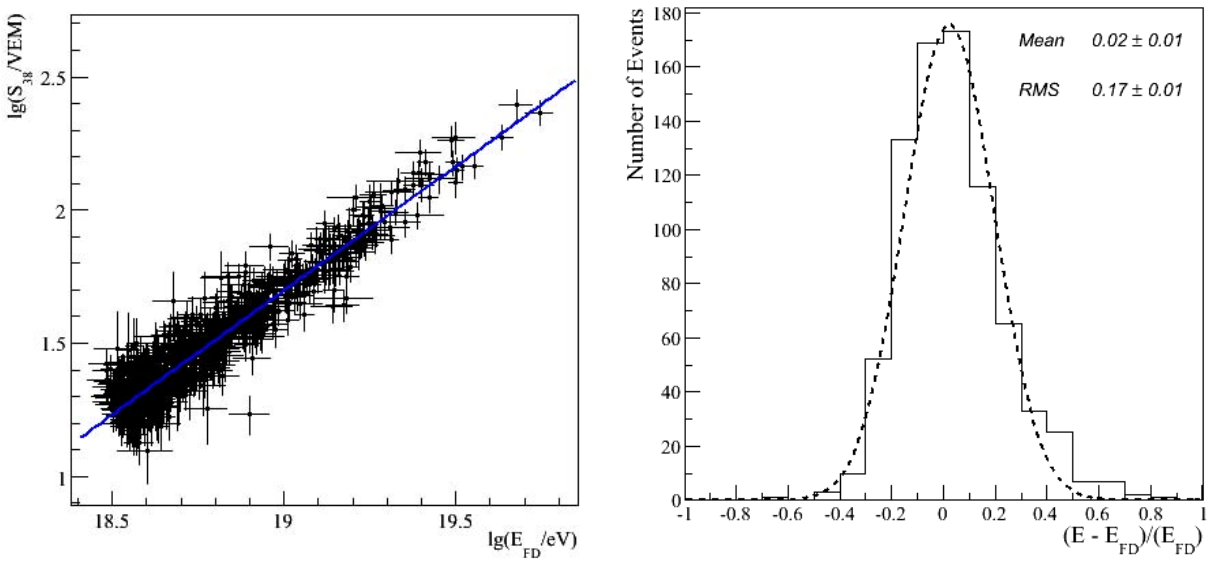

Figure 18. The calibration of the energy estimator S_{38} using the calorimetric energy from the FD is shown in the left panel, together with the result of the fit described in the text. The overall relative uncertainty of the energy (rms value 17%) is shown in the right panel.

The energy calibration, as obtained from the subset of hybrid events (see figure 18), is then used for the full set of events with the higher statistics that is measured by the SD.

On average, the statistical error of S_{38}, as derived from the LDF fit, is about 14%, decreasing slowly with energy (from 16% at 3×10^{18} eV to about 11% at 3×10^{19} eV), while the statistical error of E_{FD}, as derived from the Gaisser–Hillas fit, is about 9%. The spread of the data points around the fitted line in figure 18 has an rms value of 17%, which is what was expected from the quadratic combination of the two independent uncertainties on S_{38} and E_{FD} quoted above.

The Auger method for the absolute calibration of the shower's energy is at present affected by a systematic error of ±22%. The main uncertainties are due to the reconstruction method of the shower profile (about 10%), to the calibration of the FD telescopes (9%) and to the fluorescence yield (14%).

5. The Auger energy spectrum

Two different methods have been used by the Auger collaboration to measure the energy spectrum of primary cosmic rays. The data presented here refer to showers with a zenith angle below 60°, because the analysis of more inclined showers requires a more complex and sophisticated treatment.

It is experimentally known that most primaries are nuclear particles. In fact, in the energy region $\sim 10^{18}$–10^{19} eV, no photon candidates were found and an upper limit of 2–3% for the photon fraction has been published in [32] by the Auger collaboration.

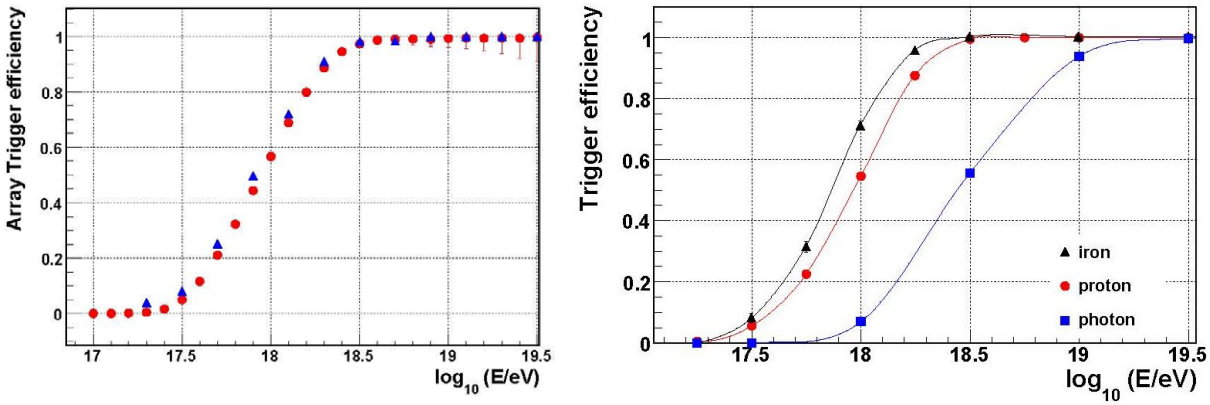

Figure 19. Left panel: the trigger efficiency of the surface array, as derived from SD data (blue triangles) and from hybrid events (red points), is shown as a function of the reconstructed shower energy. Right panel: the trigger efficiency of the surface array, as obtained from a Monte Carlo simulation for three different species of the primaries (iron nuclei, protons and photons), is shown versus the shower energy.

5.1. Data from the SD

The trigger efficiency of the SD [33], defined as the probability of triggering a shower event with the core inside the fiducial volume of the array, was determined using real events. It is shown as a function of energy in the left panel of figure 19. The blue triangles are obtained from real showers observed by the SD, including the effect of the fluctuations, whereas the red points are derived from hybrid events. It is found that the trigger efficiency goes to saturation at the energy $E \sim 3 \times 10^{18}$ eV.

These results are confirmed by a Monte Carlo simulation shown in the right panel of figure 19. For primaries with nuclear interactions, the efficiency saturates at $E \sim 3 \times 10^{18}$ eV. At higher energies, the acceptance is independent of the primary composition and determined only by the extension of the surface array. Therefore, the exposure is essentially a geometric quantity that could be calculated accurately even during the period of deployment of the SD array.

To ensure adequate containment of the event inside the array, a trigger criterion was applied, requiring that the detector giving the strongest signal should have all of its six closest neighbors fully operational.

Preliminary data for an integrated exposure of about 7000 km^2 sr yr were reported in 2008 [34]. For the results presented here, which cover the data for the period from January 2004 to December 2008, the exposure is 12 790 km^2 sr yr with an uncertainty of 3%. The energy spectrum is derived from a sample of about 35 000 events.

5.2. Hybrid data

The fluorescence detector intrinsically has the capability of measuring showers at energies lower than the SD. The present data are based on the monocular events (showers observed by only one telescope). For these events, the 'shower detector plane', defined as the plane containing the axis

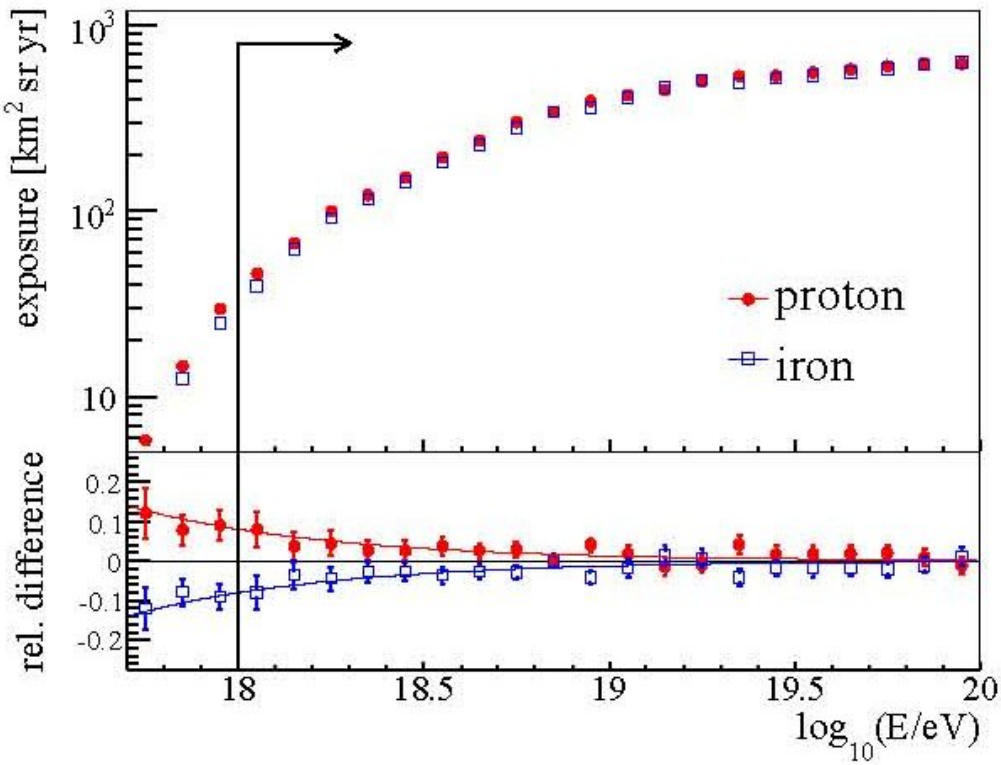

Figure 20. Exposure for the set of hybrid events as a function of energy for protons and iron nuclei from simulation. The relative difference with respect to the mean of protons and iron is shown in the bottom panel.

of the shower and the telescope, is very well measured. However, the direction of the shower axis that is lying in this plane can generally be affected by a sizeable uncertainty.

For a good geometrical reconstruction of the monocular events, additional information from the SD is needed [24]. Even the presence of a single SD activated by the shower is sufficient to locate precisely the axis of the shower in the 'shower detector plane'. The hybrid spectrum [35] is obtained from a sample of showers detected by a fluorescence telescope and by at least one SD unit.

The exposure for hybrid events was calculated with a Monte Carlo simulation, taking into account the various atmospheric effects, which have reduced the uptime fraction of the instrument. The result is shown as a function of energy in figure 20.

The exposure is found to depend on the particle composition by less than 10% for $E > 10^{18}$ eV.

This simulation of the FD exposure was validated by taking real SD events as a trigger for the hybrid chain. The FD detection probability was then evaluated and compared with the number of actually recorded real hybrid events. Agreement at the 4% level was found.

The Auger hybrid spectrum contains about 1700 events for $E > 10^{18}$ eV. The minimum energy reachable with hybrid events is substantially lower than that of the SD spectrum. This enables the feature of the spectrum called the ankle to be studied.

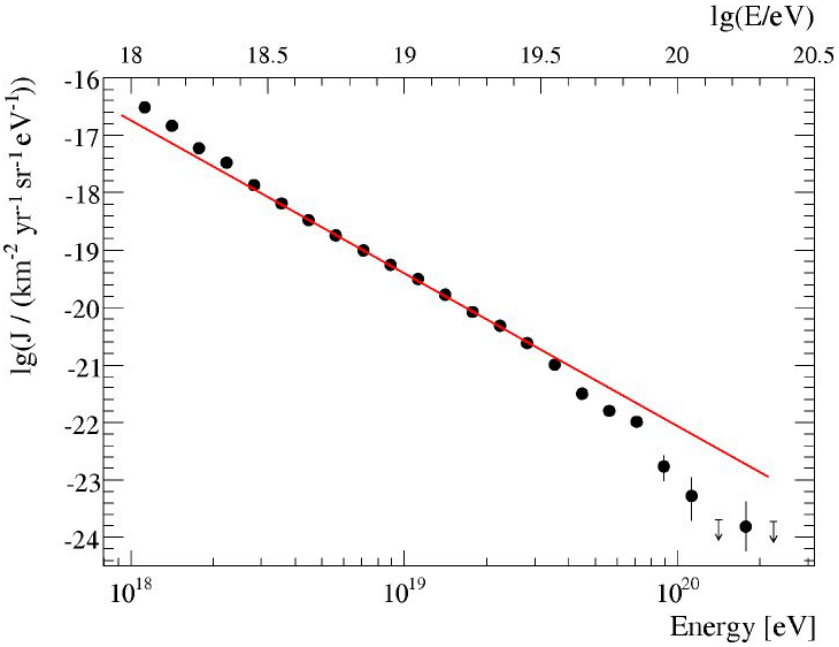

Figure 21. The combined energy spectrum from the Auger Observatory. The total number of events is about 37 000. The red line drawn through the data in the central region is only meant to give a qualitative indication of the two features (the ankle and GZK suppression).

5.3. The combined energy spectrum

The energy calibration, based on the FD calorimetric measurement, is the same for both methods described in sections 5.1 and 5.2, therefore the two spectra can be combined together. However, the energy of the hybrid data has a statistical uncertainty of about 9%, while the energy of the SD data has a 17% uncertainty, therefore the SD data have to be unfolded before combination.

The SD unfolded spectrum and the hybrid spectrum were found to be consistent within errors in the overlapping region. The resulting combined spectrum [35], shown in figure 21, clearly exhibits the two features: the ankle and GZK suppression.

A simple way of describing quantitatively the energy dependence of the spectrum in the three regions separated by the two breaking points is by a three-power-law fit, which is done by also leaving as free parameters the two values of the energy where the spectral index changes. Numerical values of the spectral index γ in the different energy intervals are given in table 1, while the corresponding fit is shown in figure 22.

The high-energy suppression that is observed above E_{GZK} is statistically very significant, being at the level of more than eight standard deviations.

The fit with three-power-law expressions is useful to characterize the energy dependence in the three different regions, but it is clearly unrealistic because of the assumed abrupt change of slope. A better functional form is obtained with two-power-law forms damped at high energy by a Fermi-type function [35]. The result is presented in figure 23, where the HiRes data are also shown for comparison.

The difference between the results from the Auger and HiRes collaborations is most likely attributable to the fact that the two experiments use different energy calibrations. In fact,

Table 1. Results of the three-power-law fit in the three energy regions separated by E_{ankle} and E_{GZK}.

Auger spectrum fit 3-power law fit $E^{-\gamma}$	
γ_1	3.26 ± 0.04
$\log(E_{\text{ankle}}/\text{eV})$	18.61 ± 0.01
γ_2	2.59 ± 0.02
$\log(E_{\text{GZK}}/\text{eV})$	19.46 ± 0.03
γ_3	4.3 ± 0.2

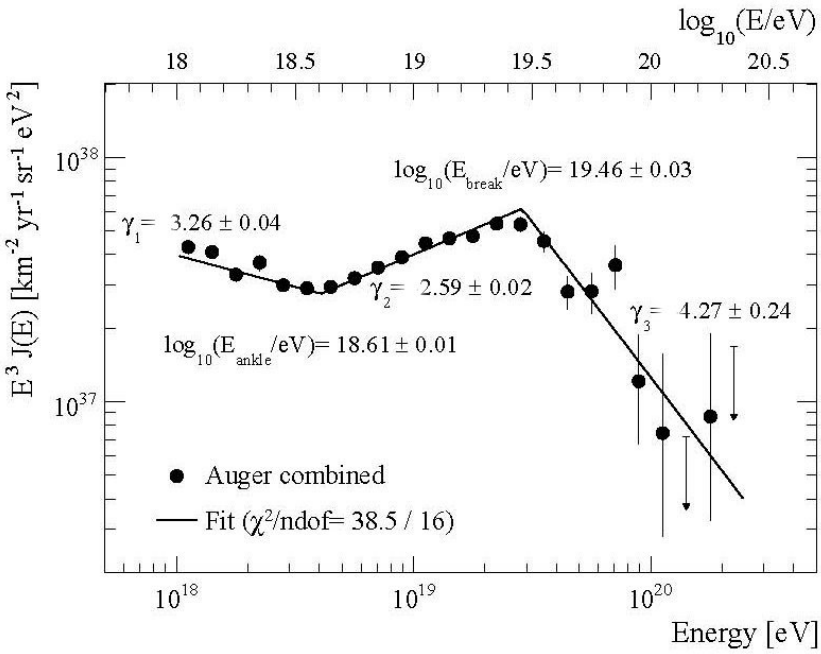

Figure 22. The Auger data presented as flux $\times E^3$ are plotted as a function of energy. Results of the three-power-law fit in the three energy regions separated by E_{ankle} and E_{GZK} (E_{break} in the figure) are shown.

applying to the data a relative shift of the energy scale by the constant, energy-independent factor of 25% would essentially bring the two sets of data into agreement.

This 25% difference in the energy scale is presumably due to the reconstruction method of the shower profile and to the absolute calibration of the fluorescence telescopes. The effect of different values used for the fluorescence yield is less than 5%.

The Auger data presented in figure 23 are shown again in figure 24 (see [36]), where they are compared with the predictions discussed in [13]. The energy spectrum at the source is assumed to follow a power law, and the effect of the interactions with the photon background during propagation is calculated. Results for both protons and iron nuclei are presented.

Within the present limited statistics, the shape of the Auger spectrum confirms the prediction of the GZK suppression for either protons or iron nuclei. This clear observation of the GZK cutoff is by itself a strong indication of the extragalactic origin of the cosmic rays at the very end of the spectrum.

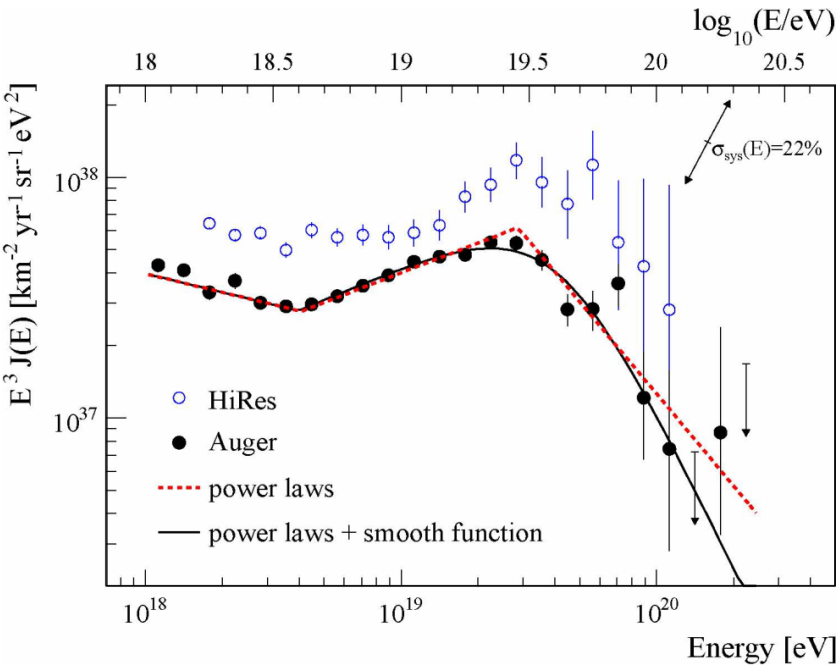

Figure 23. The Auger data presented as flux $\times E^3$ are plotted as a function of energy. The three-power-law fit is represented by the red dotted line. The black line shows a fit with a smoothing function. The 22% systematic error on the energy scale is indicated. The HiRes data are also shown for comparison.

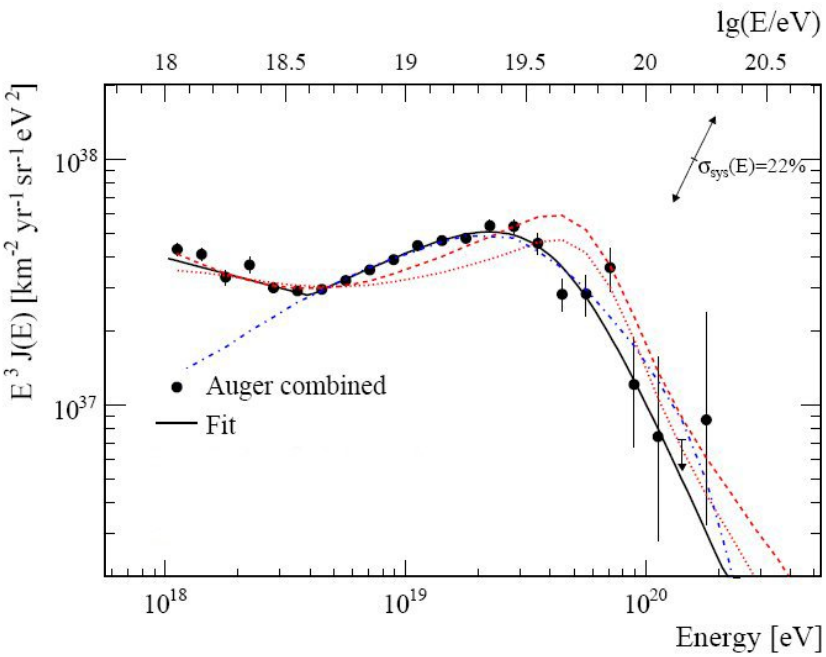

Figure 24. The energy spectrum from the Auger Observatory presented as flux $\times E^3$ is compared with different predictions from propagation models derived from [13]. The red lines refer to protons and the blue line to iron nuclei.

6. Conclusions and outlook

The Auger collaboration has presented a first measurement of the energy spectrum extending over the full energy interval explored by the observatory ($E > 10^{18}$ eV). The feature known as the ankle is clearly observed in the data. The suppression at the far end of the spectrum is consistent with the expectations from the GZK mechanism and confirms earlier data from HiRes.

Strictly speaking, the actual shape of the energy spectrum could also be affected by a reduction in the acceleration potentiality of the sources. However, disentangling this effect from the GZK cutoff appears very problematic at present.

A first attempt to identify the sources of the very-high-energy particles in the GZK region has been published by the Auger collaboration [37]. Indication of a correlation of the direction of the events having energies above $\sim 5.5 \times 10^{19}$ eV with the AGN galaxies within the GZK sphere was reported.

In the high-energy region around and above the ankle, where most or all the events are supposed to be of extragalactic origin, the energy spectrum contains basic but also complex information. In fact, this is the result of the production mechanism and of propagation effects.

Accurate measurements of the mass composition could provide useful information to discriminate between different models, but they rely on the extrapolation of hadronic physics at energies much above those explored by accelerators (LHC included). In addition, the mass composition may change during propagation.

At present, the Auger spectrum contains about 500 events in the region above the beginning of the GZK suppression. This sample is integrated over all the observed region of the sky.

During the lifetime of the observatory, these statistics will be improved by nearly one order of magnitude, thus enabling the study of the shape of the spectrum from different regions of the sky. This should provide invaluable information about the correlation of the sources with the distribution of matter within the GZK horizon. The much larger amount of data that could be collected by the Northern Auger Observatory (seven times larger than Auger South) would represent a remarkable improvement.

In perspective, the study of the energy spectrum from different regions of the sky enables a comparison of the region of the supergalactic plane with respect to other regions of the sky, and this will probably be the most unambiguous and unbiased way of understanding the origin of extragalactic rays.

References

[1] Swordy S 2001 *Space Sci. Rev.* **99** 85
[2] Engel R 2009 private communication
Blümer J *et al* 2009 *Prog. Part. Nucl. Phys.* **63** 293
[3] Cocconi G 1956 *Nuovo Cimento* **3** 1433
[4] Hillas A M 1984 *Annu. Rev. Astron. Astrophys.* **22** 425
[5] Linsley J 1963 *Phys. Rev. Lett.* **10** 146
[6] Nagano M and Watson A A 2000 *Rev. Mod. Phys.* **72** 689
[7] Greisen K 1966 *Phys. Rev. Lett.* **16** 748
Zatsepin Z T and Kuz'min V A 1966 *JETP Lett.* **4** 78
[8] Cronin J W 1992 *Nucl. Phys.* B (*Proc. Suppl.*) **28B** 213
[9] Berezinsky V and Grigoreva S I 1988 *Astron. Astrophys.* **199** 1

[10] Berezinsky V *et al* 2006 *Phys. Rev.* D **74** 043005
[11] Stanev T *et al* 2000 *Phys. Rev.* D **62** 093005
Stanev T 2009 *New J. Phys.* **11** 065013
[12] Armengaud E *et al* 2005 *Phys. Rev.* D **72** 043009
Aloisio R *et al* 2008 arXiv:0803.2494 [astro-ph]
[13] Allard D *et al* 2008 JCAP **0810**(2008)033 arXiv:0805.4779 [astro-ph]
[14] Globus N, Allard D and Parizot E 2008 *Astron. Astrophys.* **479** 97
Allard D 2009 private communication
[15] Takeda M *et al* 2003 *Astropart. Phys.* **19** 447
Shinozaki K *et al* 2006 *Proc. Quarks 2006*
[16] Abbasi R U *et al* 2008 *Phys. Rev. Lett.* **100** 101101
[17] Allard D, Parizot E and Olinto A V 2007 *Astropart. Phys.* **27** 61
[18] Unger M 2008 arXiv:0812.2763 [astro-ph]
[19] Harton J L 2009 *Proc. 31st ICRC* (*Łódź, Poland*) arXiv:0906.2354 [astro-ph]
[20] Abraham J *et al* 2004 *Nucl. Instrum. Methods* A **523** 50
[21] Allekotte I *et al* 2008 *Nucl. Instrum. Methods* A **586** 409
[22] Kamata K and Nishimura J 1958 *Suppl. Prog. Theor. Phys.* **6** 93
Greisen K 1956 *Prog. Cosmic Ray Phys.* **3** 1
[23] Newton D *et al* 2007 *Astropart. Phys.* **26** 414
[24] Abraham J *et al* 2010 *Nucl. Instrum. Methods* A at press arXiv:0907.4282v1 [astro-ph]
[25] Baltrusaitis R M *et al* 1985 *Nucl. Instrum. Methods* A **240** 410
[26] Arqueros F *et al* 2009 *New J. Phys.* **11** 065011
[27] Nagano M *et al* 2004 *Astropart. Phys.* **22** 235
See also Nagano M 2009 *New J. Phys.* **11** 065012
[28] Brack J T *et al* 2004 *Astropart. Phys.* **20** 653
[29] BenZvi S Y *et al* 2009 *Proc. 31st ICRC* (*Łódź, Poland*) arXiv:0906.2189 [astro-ph]
[30] Di Giulio C 2009 *Proc. 31st ICRC* (*Łódź, Poland*) arXiv:0906.2189v2 [astro-ph]
[31] Hersil J *et al* 1961 *Phys. Rev. Lett.* **6** 22
[32] Abraham J *et al* 2009 *Astropart. Phys.* **31** 399
[33] Abraham J *et al* 2010 *Nucl. Instrum. Methods* A **613** 29
[34] Abraham J *et al* 2008 *Phys. Rev. Lett.* **101** 061101
[35] Abraham J *et al* 2010 *Phys. Lett.* B **685** 239
[36] Schüssler F 2009 *Proc. 31st ICRC* (*Łódź, Poland*) arXiv:0906.2189v2 [astro-ph]
[37] Abraham J *et al* 2008 *Astropart. Phys.* **29** 188
Aublin J and Hague J D 2009 *Proc. 31st ICRC* (*Łódź, Poland*) (arXiv:0906.2347v2 [astro-ph])